Meccanica (2014) 49:1177–1191
DOI 10.1007/s11012-013-9861-1

Elastoplastic contact of rough surfaces: a line contact model for boundary regime of lubrication

W. W. F. Chong · M. De la Cruz

Received: 12 April 2013 / Accepted: 9 December 2013 / Published online: 8 January 2014

Abstract This paper introduces an improved friction model accounting for elastoplastic behavior of interacting asperities along contiguous rough surfaces for a line contact solution. It is based on Greenwood and Tripp's original boundary friction model and specifically tailored for a boundary regime of lubrication. The numerical solution of Reynolds' equation is achieved by implementing Elrod's cavitation algorithm for a one dimensional line contact. The transience in the numerical solution is retained by accounting for the squeeze film term in Reynolds' equation under fixed loading conditions and varying sliding motion. A sliding bearing rig is used to measure friction and compare the results with the prediction made using the approach highlighted above. The numerical/experimental results show good agreement.

W. W. F. Chong (✉)
Faculty of Engineering and the Environment, University of Southampton Malaysia Campus (USMC), Nusajaya, Johor, Malaysia
e-mail: w.chong@soton.ac.uk

W. W. F. Chong
National Centre of Advanced Tribology (nCATS), Faculty of Engineering and the Environment, University of Southampton, Southampton, UK

M. De la Cruz
Wolfson School of Mechanical & Manufacturing Engineering, Loughborough University, Loughborough, UK

Keywords Elastoplasticity · Elrod's Cavitation Algorithm · Boundary lubrication · Slider bearing

Nomenclature

D	Influence coefficient (–)
E^*	Reduced modulus of elasticity (Pa)
F	Residual function (–)
H	Non-dimensional elastic film shape (–)
H_G	Limiting average pressure (Pa)
J	Jacobian matrix (–)
L	Length of contact geometry (m)
N	Number of grid points (–)
R_x	Contact geometry equivalent curvature radius (m)
S	Squeeze term (–)
S_y	Yield strength (Pa)
W_h	Hertzian load (N)
X	Non-dimensional contact length domain (–)
Z	Viscosity-pressure index (–)
a_c	Critical contact radius (m)
c	Crown height (m)
d	Gap between two rough surface reference planes (m)
dA_a	Single asperity contact area (m^2)
dA_{act}	Total asperity/Actual contact area (m^2)
dA_{app}	An element of apparent contact area (m^2)
$d\delta$	Deflection for a single asperity contact (m)
df_v	Viscous friction for an element of apparent contact area (N/m^2)
df_b	Boundary friction for an element of apparent contact area (N/m^2)

df_{tot} Total friction for an element of apparent contact area (N/m^2)
dP_a Single asperity contact load (N)
dP_c Critical contact load (N)
dW_{act} Total asperity contact load (N)
g Switch function (–)
h Elastic film shape (m)
h_0 Undeformed central lubricating film thickness (m)
i, j Points along contact domain (–)
p Contact pressure (Pa)
p_c Cavitation pressure (Pa)
s Initial contact profile (m)
t Time domain (s)
u_{av} Lubricant entraining speed (m/s)
w_p Asperity inteference (m)
x Contact length domain (m)
$\bar{z}$ Non-dimensional individual asperity height (–)
z Individual asperity height (m)
α Viscosity coefficient (Pa^1)
α_0 Viscosity coefficient at $p = 0$ and 60 °C (Pa^1)
$\bar{\beta}$ Non-dimensional lubricant bulk modulus (–)
β Lubricant bulk modulus (Pa.s)
β_{eq} Equivalent asperity curvature radius (m)
δ^* Non-dimensional asperity deflection, $d\delta/\delta_c$ (–)
δ Elastic deformation (m)
i_c Critical deflection (m)
δ_t Deflection transition from elastic-elastoplastic (m)
η Lubricant viscosity (Pa.s)
η_0 Lubricant viscosity at $p = 0$ and 60 °C (Pa.s)
κ Pressure coefficient for boundary shear strength (–)
v Poisson's ratio (–)
ω Relaxation factor (–)
ϕ_0 Asperity distribution (–)
$\bar{\rho_c}$ Non-dimensional lubricant density at $p = p_c$ and constant temperature (–)
ρ Lubricant density (kg/m^3)
ρ_c Lubricant density at $p = p_c$ and constant temperature (kg/m^3)
ρ_0 Lubricant density at $p = 0$ and constant temperature (kg/m^3)
σ RMS surface height (m)
τ Lubricant shear stress (Pa)
τ_0 Eyring limiting shear stress (Pa)
θ Fractional film content-Cavitation, if $\theta < 1.0$ (–)
θ Non-dimensional density-Full Film, if $\theta \geq 1.0$ (–)
ξ Surface density of asperity peaks (–)

1 Introduction

A multi-scale physical approach is required to understand the tribological characteristics of engineering conjunctions such as cam-tappet and piston ring/liner contacts. For example, in the piston ring/liner conjunction, piston speed at macroscopic level dominates the kinematics of the contact. The ring-liner conjunction is at microscopic level and ensures the formation of a thin lubricant film, which for the most parts inhibits direct contact of the surfaces and hence reduces friction. However, the thickness of the lubricant film formed depends on the kinematics of the piston motion, leading to a multi-scale contact problem. At low sliding speeds coupled with heavy load, the ring/liner contact might even undergo mixed lubrication (Fig. 1), inducing higher friction as a result of direct surface asperity interactions.

The Stribeck curve only provides an indication of the regime of lubrication, based upon the ratio of lubricant film thickness to the asperity heights on the counterface surfaces (Fig. 1). Evidently, in order to predict friction between nominally lubricated sliding surfaces, one must first be able to predict the lubricant film thickness. The most commonly used approach is to compute the film thickness and contact pressure distribution through solution of Reynolds' equation [1] using the Swift-Stieber exit boundary conditions [2, 3].

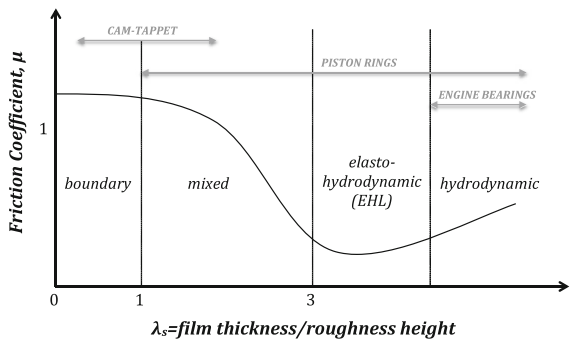

Fig. 1 Lubrication regimes for various engineering applications—Stribeck curve

Since the inception of Reynolds' equation [1] in 1886, various modifications have been proposed in order to suit it to particular conditions or include certain salient features of analysis. For instance, Reynolds' equation is adopted to include the influence of two phase flow or cavity formation by Elrod [4]. Recently, Chong et al. [5] proposed a modified Elrod's cavitation algorithm to predict contact pressure and film thickness along the piston ring/liner conjunction. The model is extended for use in applications such as transmission gear contact [6] and cam-tappet conjunction [7]. Patir and Cheng [8, 9] also modified the Reynolds' equation for rough surfaces, taking into consideration shear flow factors as a result of lubricant entrainment across surface features. Rahmani et al. [10], based on Patir and Cheng's approach, proposed an analytical solution to study the influence of surface texturing on the friction of slider bearings. Their approach is recently extended to predict friction along the ring/liner conjunction [11].

Lubricant film thickness for typical engineering applications, such as piston ring/liner conjunction, is normally in the range of a few micrometers. At such scale, engineering surfaces are rough. Randomly distributed peaks (known as asperities) and valleys combine to form the roughness of a surface. Along mixed lubrication regime, the lubricant film thickness is comparable to the height of these surface features. Mechanisms contributing to friction include: (1) viscous friction and (2) boundary friction. As the contact tends to boundary interactions, the latter becomes more significant. Greenwood and Williamson [12] proposed one of the earliest rough surface contact models, valid for engineering applications and for the fundamental theories of elastic contact and friction. The model showed dependency of the contact on the topography of the surface. Greenwood and Tripp [13] demonstrated that an equivalent single rough surface model can always be found, which predicts the same behaviour as that of a two-rough surface model (e.g. Greenwood and Williamson approach [12]).

Regardless of the geometrical size of the contact, the asperity contact area (summation of all contacting asperities) is significantly smaller than the apparent contact footprint, often introducing localised high compressive stresses at each asperity pair contact. This can induce asperity level yielding, possibly leading to plastic deformation and wear. However, both the rough surface models mentioned above assume elastic Hertzian contact for asperity pairs, which might lead to inaccuracies when predicting rough surface contact characteristics.

Fuller and Tabor [14] proposed an alternative rough surface contact model to account for adhesive contact between asperities [using Johnson, Kendall and Roberts' (JKR) contact model [15]]. Based on statistical representation of surface roughness, Chang et al. [16] derived a friction model for rough metallic surfaces taking into account surface adhesion and also plasticity. The model better known as the CEB model was later extended by Polycarpou and Etsion [17] to include sub-boundary lubrication. Using finite element analysis, Kogut and Etsion [18] derived analytical expressions to describe the elastoplastic deformation of asperity pair interaction for a Hertzian type contact. Their approach was extended to include boundary adhesion [19] using the DMT (Derjaguin et al. [20]) assumption. The model assumes that adhesion forces may be significant with respect to the contact load in the elastic region of deformation and also in the early stages of elastoplastic behaviour. However, the model is limited to the use for features of stiff materials with sufficiently small curvature radii. In a later study, Shi and Polycarpou [21] combined the Maugis-Dugdale [22] adhesion model for elastic region with the elasto-plastic adhesion model together with the Lennard-Jones potential to consider the existence of a thin layer of lubrication film along rough surface interactions.

Jackson and Green [23] also proposed a set of expressions to describe the elastoplastic deformation of a sphere contacting a rigid semi-infinite flat plane. Their model was developed in a manner which would be useful for both macro-scale and also micro-scale contacts. The von Mises criterion was used to describe yielding of the material. The model embeds the elastoplastic deformation of a single asperity pair contact in the expressions which were eventually derived. On the other hand, Green [24] and Vijaywargiya and Green [25] studied the elastoplasticity deformation of dry sliding cylindrical contacts. These models could also be adapted for asperity level contacts if necessary. Adapting the fractal approaches proposed by Yan and Komvopoulos [26] and later extended by Morrow and Lovell [27] for rough surface adhesion, Chong et al. [28] applied the elastoplasticity

deformation asperity model proposed by Jackson and Green [23] to predict friction in fractal-represented surfaces. They considered nano-scale wet asperity interactions using a molecular level simulation via statistical mechanics for idealised fluid molecules [29, 30].

From an experimental perspective, there are plenty of ready made tribometers that can be used to measure friction of sliding surfaces. These vary from a pin-on-disk friction machine [31] to low frequency reciprocating wear testers [32], high frequency oscillatory rubbing wear [32], Cameron-Plint T-77 [33], to name but a few. Other authors have developed in-house rigs to meet their specific requirements [34, 35], allowing for a greater flexibility of use and development. It seems appropriate, then, that a rig tailored to the specific operating conditions of boundary friction had to be developed.

As an initial approach to predict friction more accurately, the current study proposes an integrated modified Elrod's algorithm with a modified Greenwood and Tripp model for a line contact sliding bearing configuration. The aim of the study is to validate the friction computed, based upon the proposed model using a precision sliding bearing mechanism. The model predicts the thickness of the lubricating film and also includes a modified elasto-plasticity model for asperity interactions along rough surfaces for the studied line contact problem, which considers the transition of the asperity contact deformation from elastic to elastoplastic and finally fully plastic states.

2 Mathematical model

2.1 Contact conjunction

In this study, the shearing of the lubricant film in the contact conjunction (Fig. 2) is predicted through a simultaneous one-dimensional solution of Elrod's equation and the elastic film shape. The length-to-width ratio of the experimental sliding strip is large, thus a one-dimensional solution of Elrod's equation is assumed in the direction of the contact face-width, x. Ignoring any side leakage of the lubricant film normal to the direction of the entraining motion, then [4]:

$$\frac{\partial}{\partial x}\left[\frac{\rho_c h^3}{\eta} g\beta \frac{d\theta}{\partial x}\right] = 12\left\{\frac{\partial}{\partial x}[\theta\rho_c h(u_{av})] + \frac{d}{dt}(\theta\rho_c h)\right\} \tag{1}$$

where $d(\theta\rho_c\ h)/dt$ refers to the squeeze film term, making for a transient analysis of the studied problem. The instantaneous contact kinematics is due to the speed of entraining motion, u_{av} and the squeeze film velocity, dh/dt. The time history of any formed lubricant film is, therefore, retained. The inclusion of this term also takes into account the vertical floatation of the ring strip, as described in Sect. 3.

To include the effect of cavitation at the trailing edge of the contact, Elrod [4] defined the contact pressure, p as a result of a fluid film, comprising some liquid lubricant content, θ. The implication in Elrods definition is that some fraction of the lubricant film content may be as a result of vapour or gaseous medium below the lubricant vaporisation/cavitation pressure, p_c. Therefore,

$$p = g\beta \ln\theta + p_c \tag{2}$$

with β being the lubricant bulk modulus. The term g is the switching term and can be expressed as:

$$g = \begin{cases} 1 \Rightarrow & \text{Full film, if } \theta \geq 1 \\ 0 \Rightarrow & \text{Cavitation, if } 0 < \theta < 1 \end{cases} \tag{3}$$

when $0 < \theta < 1$, the switching term $g = 0$, suggesting a two-phase flow below cavitation pressure.

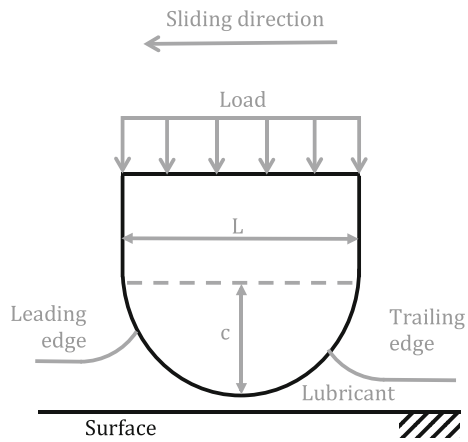

Fig. 2 Sliding contact

The elastic film shape, h is:

$$h(x) = h_o + s(x) \tag{4}$$

With the initial contact profile, $s(x)$ being defined as:

$$s(x) = \frac{cx^2}{(L/2)^2} \tag{5}$$

The lubricant viscosity–pressure variation can be predicted using the Roelands' equation [36]:

$$\eta = \eta_o e^{\alpha} \tag{6}$$

where $\alpha = (\ln \eta_o + 9.67)\{[1 + p/(1.98 \times 10^8)]^Z - 1\}/p$ and $Z = \alpha_o/[5.1 \times 10^{-9}(\ln \eta_o + 9.67)]$.

Lubricant density variation with contact pressure, p is given by Dowson and Higginson [37] as:

$$\rho = \rho_o\left(1 + \frac{0.6 \times 10^{-9}p}{1 + 1.7 \times 10^{-9}p}\right) \tag{7}$$

The combined solution of Eqs. (1–7), described above, determines the contact pressure distribution, $p(x, t)$ at any instant time. The solution clearly shows that along the cavitation region ($g = 0$), the Poiseuille flow term on the left hand side of the Eq. (1) diminishes. Therefore, the mass flow rate through the cavitation region is a balance between the Couette flow as a result of lubricant film entrainment and any mutual approach or separation of contiguous surfaces.

2.2 Friction model

Engineering surfaces are microscopically rough, consisting of peaks (also known as asperities) and valleys. During contact, both surfaces of the studied conjunction are rough. Viscous friction dominates when the lubricant film is thick. However, when the lubricant film is thin and comparable to the surface roughness, asperity interaction can no longer be avoided. Hence, this would lead to boundary friction. As a result, the total friction for an element of apparent contact area, dA_{app} (=$L.dx$) is as:

$$df_{tot} = df_v + df_b \tag{8}$$

with df_b referring to the boundary friction component and df_v as the viscous friction component, the viscous friction, df_v for a Newtonian fluid can be computed as:

$$df_v = \tau\left(dA_{app} - dA_a\right) \tag{9}$$

where dA_{app} is the apparent contact area, dA_a is the actual contact area and $\tau = \eta u_{av}/h(x)$.

Boundary friction arises from shearing of a very thin film, which prevails along contacting asperity tips. This molecular thin film is non-Newtonian and can be predicted using the classical Eyring thermal-activation model [38]. Therefore, the boundary friction, df_b can be expressed as:

$$df_b = dA_{act}\left(\tau_o + \kappa\frac{dW_{act}}{dA_{act}}\right) \tag{10}$$

where τ_o referring to the Eyring shear stress of the lubricant, κ the pressure coefficient for boundary shear strength of the bounding surfaces and dW_{act} is the share of elemental contact load carried by the asperities.

Greenwood and Tripp [13] described the load carried by the asperities along a rough surface contact, dW_{act} and the actual contact area, dA_{act} as

$$dW_{act}(d) = \xi.dA_{app}\int_d^{\infty} dP_o(z-d)\phi_o(z)dz \tag{11}$$

$$dA_{act}(d) = \xi.dA_{app}\int_d^{\infty} dA_o(z-d)\phi_o(z)dz \tag{12}$$

where the term ϕ_o refers to the asperity distribution and is described as follow:

$$\phi_o(z) = \frac{1}{\sqrt{2\pi}}exp\left(-\frac{s^2}{2}\right) \tag{13}$$

The terms dP_o and dA_o are

$$dP_o(w_p) = 2\pi\xi\int_0^{\infty} dP_a(w_p - 2f(r/2), r)r.dr \tag{14}$$

$$dA_o(w_p) = 2\pi\xi\int_0^{\infty} dA_a(w_p - 2f(r/2), r)r.dr \tag{15}$$

with w_p being the asperity interference as shown in Fig. 3.

In Eqs. (14) and (15), dP_a and dA_a refer to the single asperity pair load carrying capacity and the actual asperity-pair contact area. Assuming that the asperity contact is fully elastic, Greenwood and Tripp [13] applied the Hertzian theory to compute these two parameters. They also considered an elastic-fully plastic model to describe plastic deformation of asperities in contact. However, in this study, the terms

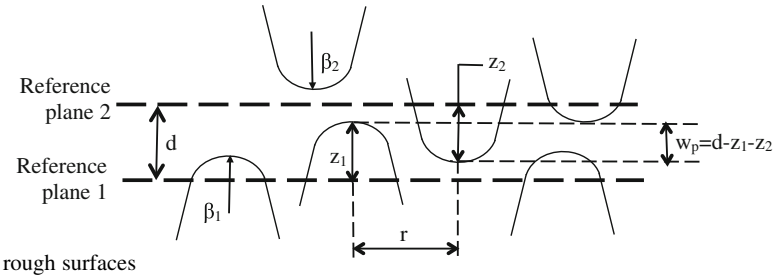

Fig. 3 Contact of two rough surfaces

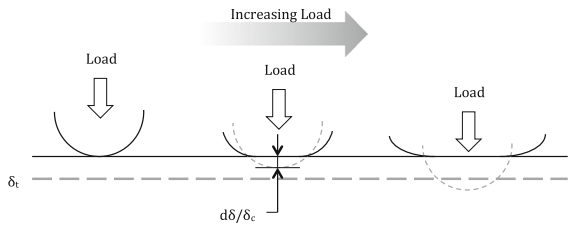

Fig. 4 Asperity deflection considering elastoplasticity deformation

dP_a and dA_a are predicted based on the approach proposed by Chong et al. [28] using the elastoplasticity model of Jackson and Green [23]. The model considers the elastoplasticity transition of contact deformation instead of assuming an elastic then fully plastic asperity deformation.

According to Chong et al. [28], when the normalised deflection $d\delta/\delta_c$ is less than the deflection transition from elastic to elastoplastic, δ_t, Hertzian theory applies for both terms of dP_a and dA_a (Fig. 4).

$$dP_a(w) = \frac{4}{3}E^*\left(\beta_{eq}\right)^{1/2}(d\delta)^{3/2} \tag{16}$$

$$dA_a(w) = \pi\beta_{eq}d\delta \tag{17}$$

when $d\delta/\delta_c \geq \delta_t$, the equations proposed by Jackson and Green [23] are applied to describe the load carrying capacity, dP_a and the actual contact area, dA_a of the asperity interaction.

$$dP_a = dP_c\left\{\begin{array}{c} e^{-0.25(\delta^*)^{5/12}}(\delta^*)^{3/2} \\ +\frac{4H_G}{CS_y}\left[1-e^{-0.04(\delta^*)^{5/9}}\right]\delta^* \end{array}\right\} \tag{18}$$

$$dA_a = \pi a_c^2\delta_t\left(\frac{\delta^*}{\delta_t\delta_c}\right)^{B+1} \tag{19}$$

The coefficients used in Eqs. (16) to (19) are explained and given in Appendix (Table 1).

From the modified Greenwood and Tripp model described above, the total friction, f_{tot} along the contact can be computed as

$$f_{tot} = \text{Ring length} \times \int_{-L/2}^{L/2} df_{tot}dx \tag{20}$$

Figure 3 also shows that under certain conditions, asperities might come into contact along the shoulders. The asperities given by Greenwood and Tripps [13] approach and also in this paper are assumed to be hemispherical, having similar curvature radii. Based on the assumption, initial contact will occur midway between the centres of opposing asperities. For the misaligned asperities, which might interact along the shoulders, the normal forces will not be acting vertically and a tangential component will exist. However, according to Greenwood and Tripp [13], the slopes of asperities along physical rough surfaces are so small that the errors are miniscule and can be ignored. Hence, this leads to the assumption that all asperities will be normally loaded.

2.3 Numerical procedure

2.3.1 Contact conjunction

The transient contact pressure distribution, $p(x, t)$ and the corresponding lubricant film thickness, $h(x, t)$ are first computed. Applying the discretisation by Chong et al. [5], Eq. (1) is written as:

$$\frac{\partial}{\partial X}\left[\frac{\bar{\rho}_c H^3}{\bar{\eta}}\frac{\partial g(\theta-1)}{\partial X}\right] = \psi\left\{\frac{\partial}{\partial X}[\theta\bar{\rho}_c H] + \frac{R_x}{b}S(\theta\bar{\rho}_c)\right\} \tag{21}$$

where $gd\theta/dx = dg(\theta-1)/dx, \psi = 12(R_x/b)^3/\bar{\beta}$ and $S = (dh/dt)/u_{av}$.

Equation (21) is then solved using the finite difference scheme suggested by Jalali et al. [39]. The Poiseuille term (left hand side of Eq. 21) is discretized using central finite differencing. This provides second order accuracy, as the solution along the full film region must consider all the neighbouring nodes. For the Couette term, which is predominant in the the cavitation region (right hand side of Eq. 21), a backward differencing scheme with first order accuracy is deployed.

The numerical algorithm is divided into two consecutive loops (a pressure and a load loop). The pressure loop uses the iterative approach proposed by Jalali et al. [39] for integrating Reynolds equation as a starting point. However, the convergence used in this study is focused on θ and the lubricant pressure is computed after the convergence is achieved. The Jacobian matrix, J for this case is expressed as:

$$J_{i,j} = \frac{\partial F_i}{\partial [g\theta]_j} \tag{22}$$

where F_i is the residual term (see Appendix 1), and i, j are grid points along the contact width. The value of θ_i^k at iteration k can be computed as:

$$\theta_i^k = \theta_i^{k-1} + \omega \Delta\theta_i^k \tag{23}$$

where ω is the relaxation factor and $\Delta\theta_i^k = -(F_i + J_{i,i-1}\Delta\theta_{i-1}^k + J_{i,i+1}\Delta\theta_{i+1}^k)/J_{i,i}$. The convergency criterion for θ is: $\sum \left(\theta_i^k - \theta_i^{k-1}\right)^{0.5}/N \leq 1.0 \times 10^{-7}$, where N is the number of mesh points ($N = 200$). In the load loop the contact load is compared with the reference load. The convergence criterion is $|\int Pdx - W|/W \leq 0.01$.

2.4 Friction model

The integrals in Eqs. (11) and (12) of the modified Greenwood and Tripp friction model are improper integrals. Therefore, to solve these equations using the Gauss–Legendre quadrature, the limits of the integral are modified as follow

$$dW_a(d) = \frac{\eta . dA_{app}}{(1-\bar{z})^2} \int_0^1 dP_o\left(\frac{\bar{z}}{1-\bar{z}}\right)\phi_o\left(d + \frac{\bar{z}}{1-\bar{z}}\right)d\bar{z} \tag{24}$$

$$dA_a(d) = \frac{\eta . dA_{app}}{(1-\bar{z})^2} \int_0^1 dA_o\left(\frac{\bar{z}}{1-\bar{z}}\right)\phi_o\left(d + \frac{\bar{z}}{1-\bar{z}}\right)d\bar{z} \tag{25}$$

where $z = d + \bar{z}/(1-\bar{z})$.

The integrals in Eqs. (14) and (15) describing both terms dP_o and dA_o have infinite intervals. Hence, these are solved numerically using the Gauss–Laguerre quadrature. The choice for solving the modified Greenwood and Tripp friction model numerically instead of finding an exact solution is to ensure flexibility in the use of desired single asperity pair interaction models in order to compute dP_a and dA_a.

3 Experimental procedures

3.1 Precision slider bearing mechanism

The experimental techniques used comprise of a purpose built friction measurement rig. The reason for building this rig is twofold. The first aspect is for the validation of the presented friction. The second area of interest is to study various surface textures and their effect on friction reduction [35]. Other studies using similar rigs are also available in literature, such as the work by Ryk and Etsion [40]. All the experimental results shown in this paper correspond to the validation of the model only.

Figure 5 presents the test rig as a series of schematic, not to scale drawings. Figure 5a is a top view of the aforementioned rig. It attempts to describe the test bed in its most generic form. The optical table where the rig is placed is shown, together with the control mechanism (CPU). The control and data acquisition systems are both written within the Labview environment. A National Instruments DAQ-card is used to send and receive data from the CPU to the rig. The encoder placed at the end of the lead screw serves two main functions: (1) acts as a feedback to the control system and (2) synchronizes the data acquisition, saving friction and speed on an encoder count base. A proportional-integral-derivative (PID) controller was introduced in an attempt to minimize response times. The direction of motion is controlled by a digital channel.

The speed is accurately captured with a two-beam laser vibrometer and the friction values are measured

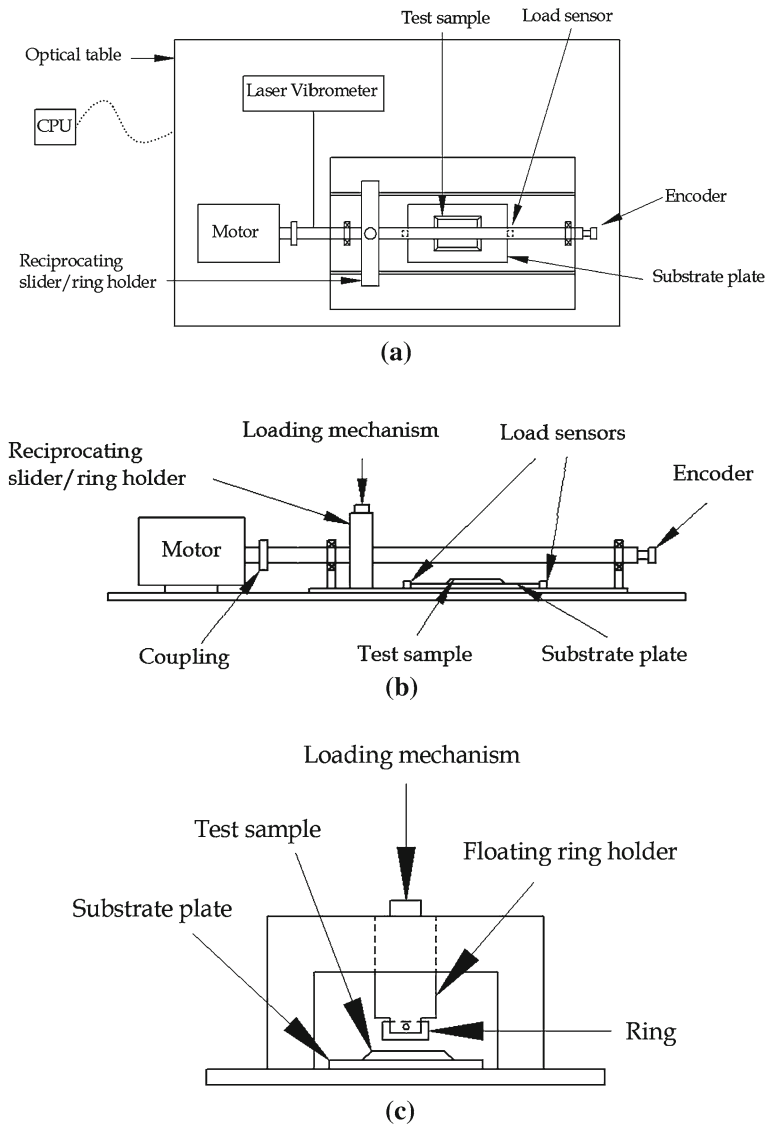

Fig. 5 Rig description, schematically presented. **a** Top view, **b** side view and **c** detail of ring holder and loading mechanism front view

with the aid of two load sensors. These are located at both ends of the substrate plate and pre-loaded to eliminate any possible excess clearances. The test sample is rigidly clamped onto the substrate plate. The reciprocating slider part holds the flat test ring.

Figure 5b shows a side view of the assembly. In this image, the test sample and substrate plates are presented in a clearer manner, together with their corresponding load sensors. Also, the loading mechanism is introduced. To further understand this function, one should refer to Fig. 5c, where a detailed view of the reciprocating slider/ring holder is shown. The test ring is attached to the floating ring holder. The ring holder is essentially a cylinder inserted onto the reciprocating slider. It is only allowed to float in the vertical direction; all other degrees of freedom are constrained. In this manner, a load can be applied, retaining the fundamental squeeze action.

The bottom plate tested is made of EN 14 steel and ground to an Rq value of 0.29 μm, with a flatness of 1 μm along the test area (26×35 mm^2). The counterpart sliding strip is made of hardened 440 C stainless steel, with a hardness of 54 Rockwell C. A parabolic profile of crown height radius 31 mm was then cylindrically ground on the face-width of the strip, resembling that of a compression ring in an

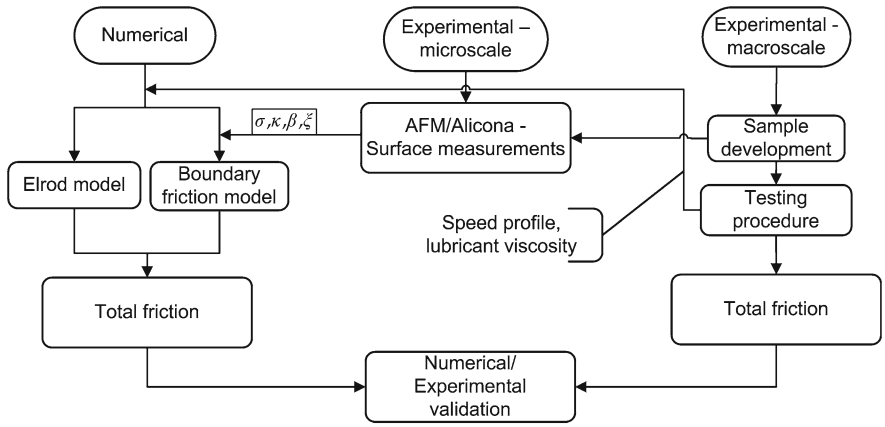

Fig. 6 Analysis approach—flow diagram

internal combustion engine piston. The roughness value of the strips profile was measured to be 0.18 μm (Rq). The overall size of the strip is set to $1 \times 31 \times 17$ mm, where the profile was introduced along the 1×31 mm edge (contact strip).

4 Results and discussions

Figure 6 illustrates the multi-scale physical approach applied in this study to predict the friction for a line contact problem. The proposed numerical model requires surface topographical parameters measured using both an atomic force microscope (AFM) and the Alicona infinite focus microscope. The friction predicted using the model is then compared with experimentally measured values for validation.

4.1 Modified Greenwood and Tripp friction model

Before proceeding to predict friction for a line contact slider bearing problem, the study first looks at the elastoplastic single asperity friction model. Figure 7a shows the actual contact area variation as a function of contact load for a single asperity contact. It is observed that with the initiation of plasticity, within the asperity contact ($d\delta/\delta_c > \delta_t$), an increase in contact load produces a larger contact area as compared with an assumed elastic contact. This contact characteristic reflects the decrease in load carrying capacity of the asperity contact once plasticity is initiated.

By distributing the single asperity contact along a rough surface using Greenwood and Tripp's approach for rough surfaces, Fig. 7b illustrates the change in the actual contact area with an increase in the applied load. The contact area predicted for the rough surface contact is larger for the elastoplastic model than that of an elastic model, which is based on Hertzian theory. This shows that the elastic deformation assumption underestimates the contact area for a given applied load when plasticity is initiated. Hence, this would produce inaccuracies in the prediction of the frictional characteristics along the rough surface contact. Figure 7c shows the contact area bearing ratio (actual contact area/apparent contact area) with respect to decreasing surface separation. Again, an elastic approach seems to be misleading, since it overestimates the separation of bodies; leading to an under-estimation of friction.

To predict friction for an element of a rough surface, an experimental value for the term κ, referring to the pressure coefficient for boundary shear strength of the bounding surfaces is required (Eq. 10). This is obtained empirically using the AFM by applying the lateral force microscopy (LFM) approach. The tip radius for the silicon nitride tip (DNP-10) is small ($\approx$60 nm) as compared to the surface roughness of the test plate ($\approx$0.33 μm). Hence, this reduces the influence of surface roughness (friction arising predominantly as a result of boundary interaction) when measuring the friction using the AFM, leading to a more accurate measurement for the κ term.

In this study, the slider rig represents a realistic contact while the AFM tip resembles an asperity contact. Hence, the Veeco 3.5 nano scope AFM with a silicon nitride tip (DNP-10) is used to measure the pressure coefficient, κ on the test plate. Calibration of

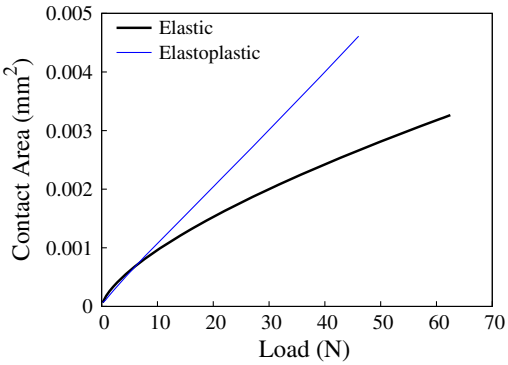

(a) Single asperity contact: Actual contact area vs Contact load

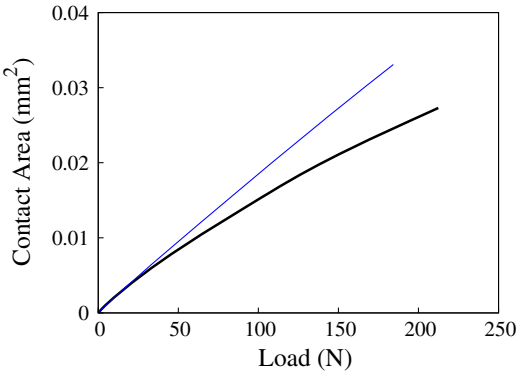

(b) Rough surface contact: Actual contact area vs Contact load

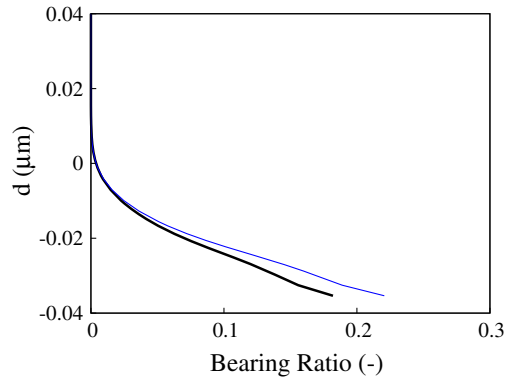

(c) Rough surface contact: Contact area bearing ratio of the rough surface contact

Fig. 7 Modified Greenwood and Tripp friction model

the tip is conducted using a silicon wafer by adopting the approach proposed by Buenviaje et al. [41]. To take into account the influence of the lubricant shear

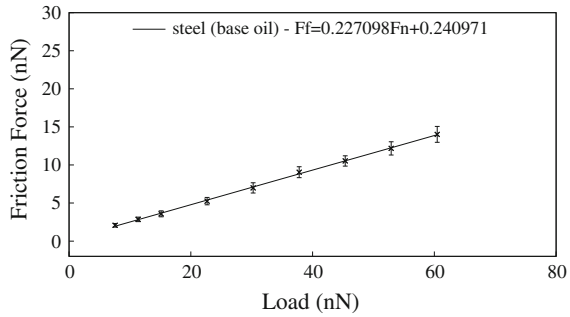

Fig. 8 Single asperity friction measurements using atomic force microscope (AFM)

along asperity interactions, it is appropriate to measure the pressure coefficient of the boundary shear strength in a lubricated condition using the fluid imaging approach for the AFM. The friction force obtained from the AFM measurements at different applied loads are plotted in Fig. 8. The slope of the friction-load curve gives the value of κ required to predict the boundary friction. One thing to note is that the intersection of the friction-load curve is neglected when defining the pressure coefficient, κ. This is because the intersection magnitude in nano-metric range will be minute compared with the applied load and is mathematically deemed to be negligible.

4.2 Numerical simulation and experimental results comparison

Using the measured contact parameters in Appendix (Table 1), the sliding speed profiles for the simulated contact as a function of encoder count, under three separate sliding conditions are shown in Fig. 9. These are used as input for the contact kinematics in the numerical model, simulating the real time experiment conditions of the contact.

Elrod's equation is solved numerically with an initially assumed elastic Greenwood and Tripp friction model. Figure 10a shows the pressure distribution of the contact peaks at different magnitudes for varying sliding speed profiles (along location **X** in Fig. 9). The reduction in peak pressure is a result of the increasing squeeze film effect with higher entraining motion of the contact, leading to a thicker lubricant film formation, hence reducing boundary friction of the contact, which is reflected in Fig. 10b, c. In them, the boundary shear component decreases significantly,

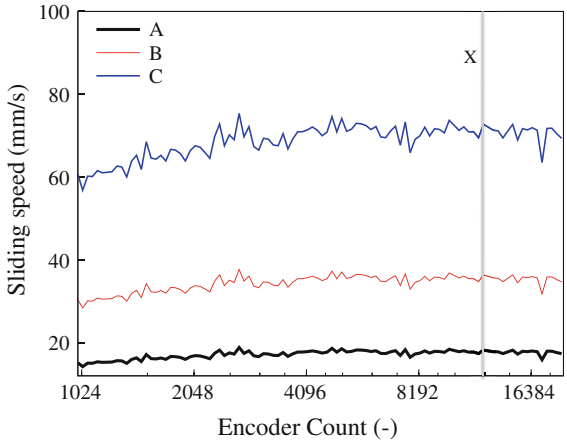

Fig. 9 Sliding speed against encoder count for the simulated cycle

while viscous shear increases with entraining speed of the contact. One thing to note is that in the cavitation region, rupture of fluid film occurs, leading to a discontinuity in viscous shear (Fig. 10b).

By plotting the friction coefficient as a function of the Stribeck oil film parameter, λ_s in Fig. 11, the simulated sliding speed profiles are observed to shift from mixed towards boundary lubrication regime as the speed decreases. The shift towards boundary lubrication is expected, because the decreasing sliding speed reduces the entrainment of lubricant into the contact, leading to a thinner lubricant film. By varying the speed, it is noted that a thicker oil film, enhancing the effect of viscous friction, may govern the conjunctional behaviour. Therefore, a much slower speed profile is preferred, where the fluid film formation is assessed by means of Elrod's cavitation algorithm, retaining the effect of elastoplasticity. The validation for the new modified Greenwood and Tripp model, presented here, is solely conducted on speed profile A, where a boundary regime of lubrication is clearly attained.

Figure 12a compares the predicted friction using the modified Elrod and the Reynolds' solution, based on the sliding speed profile A, with the measured friction values. It is observed that by assuming elastic deformation of asperities, the predicted friction by both methods (the modified Elrod and Reynolds' solution) is lower than that measured. By plotting the friction coefficient as a function of the Stribeck oil film parameter, λ_s, the experiment conducted using the

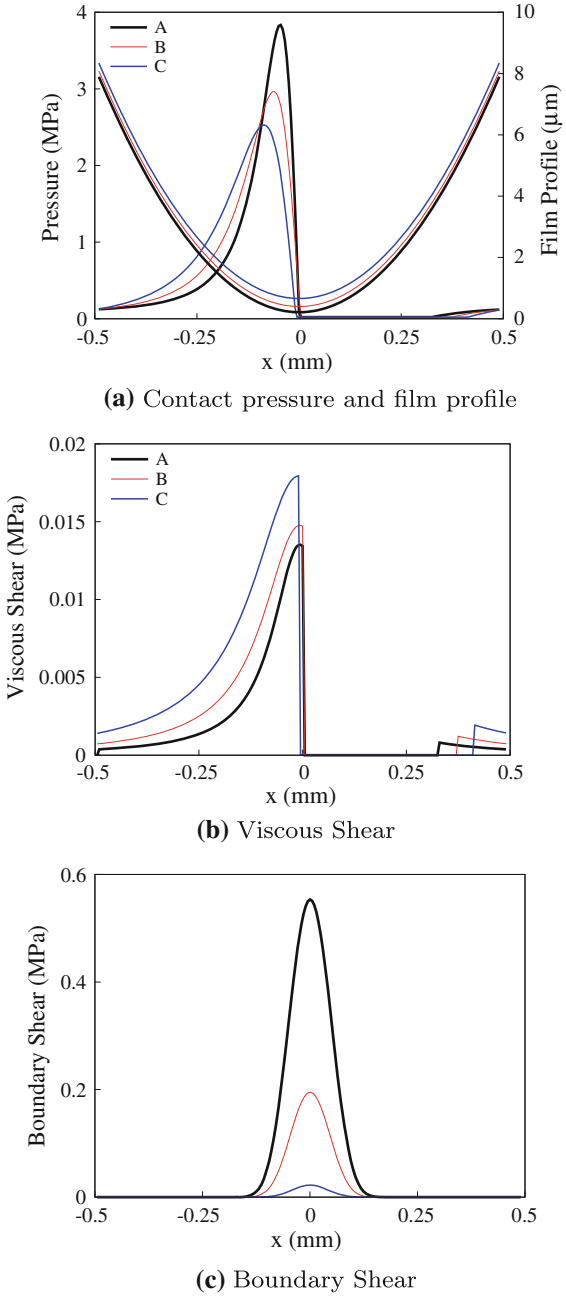

Fig. 10 Contact characteristics of the simulated problem for varying sliding speed profiles at location **X**—fully elastic assumption

precision slider mechanism is shown to be well into the boundary lubrication regime (Fig. 12b). This shows that boundary interactions of asperities dominate the underlying friction mechanism in the studied conjunction. Figure 12c plots the friction coefficient

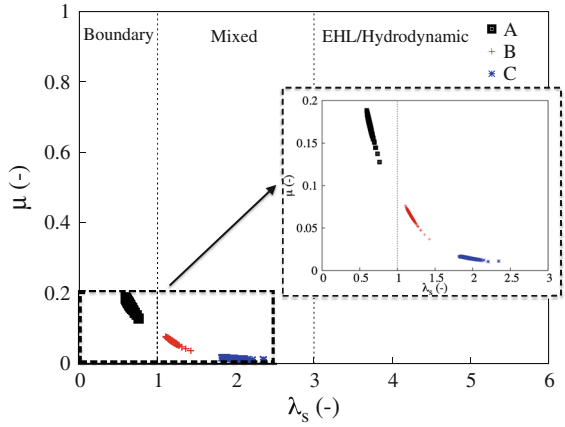

Fig. 11 Friction coefficient, μ against Stribeck oil film parameter, λ_s—fully elastic assumption

against the Stribeck number, comparing the numerical results with the experimental measurement.

Figure 12b clearly shows that the contact resides in boundary lubrication regime and it seems crucial to be able to evaluate the influence of elastoplastic deformation of the interacting asperities. Considering only the modified Elrod's solution and comparing the numerical prediction to the measured data, Fig. 13a shows that the friction force given by the elastoplastic model correlates reasonably well with the experimental values (particularly if compared to the elastic model). This indicates that elastoplastic deformation of interacting asperities plays a significant role in the frictional characteristics of the studied tribological conjunction. Figure 13b illustrates the friction coefficient in the function of the Stribeck number comparing the experimental result with the numerical ones. The boundary shear stress for both elastic and elastoplastic asperity deformation are shown in Fig. 13c. The viscous shear predicted for both friction models is the same, because the minimum film thickness given along location **X** remains unaltered. However, when elastoplasticity is considered, the boundary shear predicted increases when compared with the case of an elastic contact friction model. This is because in the operating condition investigated here, plasticity is initiated, giving a larger contact area, leading to higher contact friction. This observation is reinforced through the measured topography for the unworn and worn surfaces (Fig. 14). It is noted that in the worn surface,

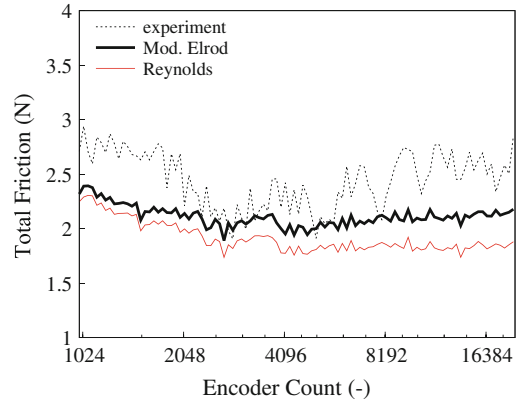

(a) Total friction against encoder count along simulated cycle

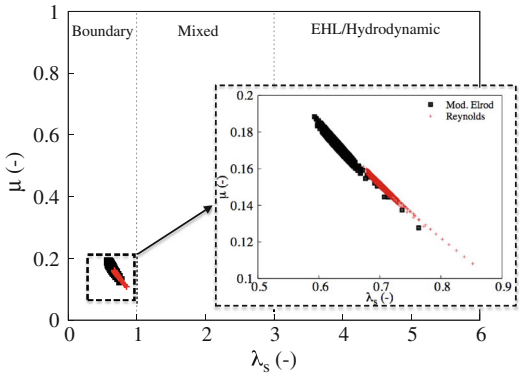

(b) Friction coefficient, μ against Stribeck oil film parameter, λ_s

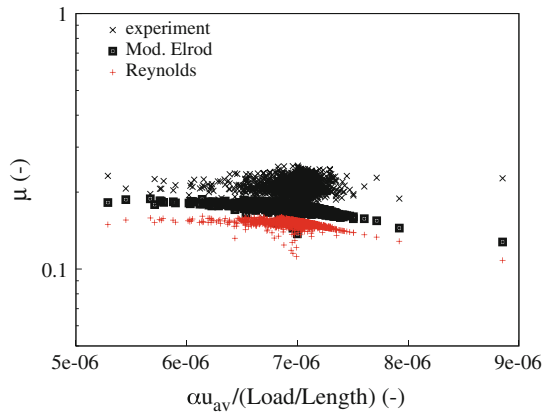

(c) Friction coefficient, μ against Stribeck number, αu_{av}/(Load per unit length)

Fig. 12 Frictional characteristics comparison between experimental measurement and numerical models (Modified Elrod and Reynolds solution) fully elastic assumption

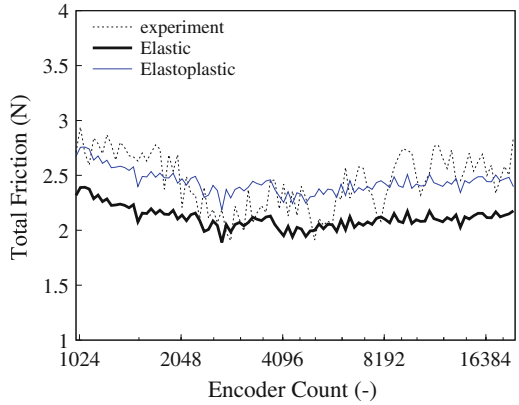

(a) Total friction against encoder count along simulated cycle

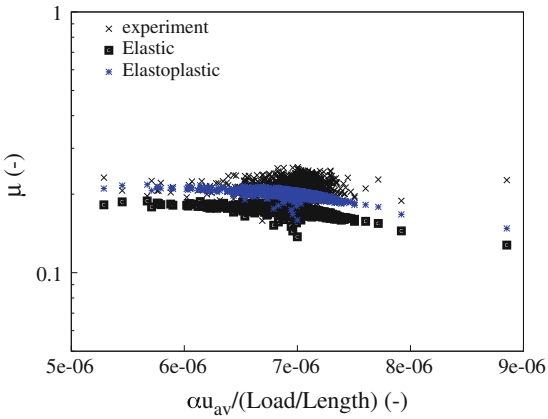

(b) Friction coefficient, μ against Stribeck number, $\alpha u_{av}/$(Load per unit length)

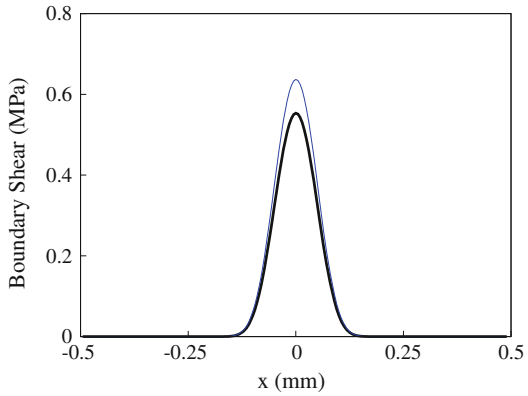

(c) Boundary Shear at location **X** (in Figure 9)

Fig. 13 Frictional characteristics comparison between experimental measurement and numerical models (elastic and elastoplastic asperity model) Modified Elrod solution

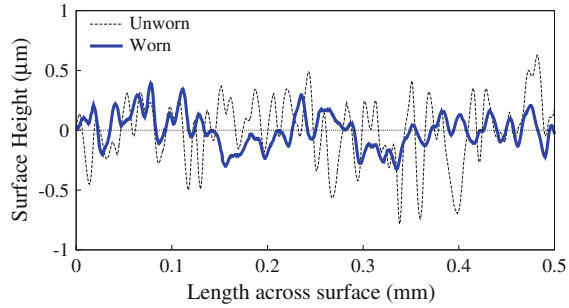

Fig. 14 Measured topography for unworn and worn surface

the asperity peaks and valleys have been smoothened, indicating a high boundary interaction of contiguous solids.

5 Conclusion

The work presented in this paper highlights the necessity of including an accurate elastoplastic model of asperity interactions. Otherwise, an underestimation of real contact area of lubricated conjunctions operating within a boundary regime of lubrication may occur. The modified Greenwood and Tripp solution has been validated against experimentally acquired friction.

The experimental results have not only been useful to validate the numerical model, but they have also shown significant plastic deformation of asperities. A purely elastic (Hertzian type) model would not be able to predict this behaviour. It is also important to note that the introduction of this model provides the opportunity of extending the work for prediction of wear.

Acknowledgements The authors acknowledge the technical support from partners and sponsorship provided by the EPSRC through the ENCYCLOPAEDIC program Grant.

Appendix

Input parameters

See Appendix Table 1.

Table 1 Measured contact parameters

Parameters	Values	Units
Contact width, L	1.0	mm
Crown height, c	8.0	μm
Cavitation pressure, p_c	0.2	MPa
Lubricant bulk modulus, β	1.72	GPa
Lubricant viscosity, η_0	0.1583	Pa.s
Pressure coefficient for boundary shear strength, κ	0.227	–
Eyring limiting shear stress, τ_0	2.5	MPa
Limiting average pressure, H_G	4.5	GPa
RMS surface height, σ	0.34	μm
$\sigma\ \xi\ \beta_{eq}$	0.0295	–
σ/β_{eq}	0.0011	–

Elastoplasticity model

$$\delta_t = 1.9$$

$$\delta^* = \frac{d\delta}{\delta_c}$$

$$\delta_c = \left(\frac{\pi C S_y}{2E^*}\right)^2 \beta_{eq}$$

$$a_c = \frac{\pi C S_y \beta_{eq}}{2E^*}$$

$$dP_c = \frac{4}{3}\left(\frac{\beta_{eq}}{E^*}\right)^2 \left(\frac{\pi C S_y}{2}\right)^3$$

$$\frac{H_G}{S_y} = 2.84\left\{1 - exp\left(-0.82\left[\frac{\pi C e_y}{2}\sqrt{\delta^*}\left(\frac{\delta^*}{\delta_t}\right)^{B/2}\right]^{-0.7}\right)\right\}$$

$$C = 1.295 \times exp(0.736v)$$

$$B = 0.14 \times exp(23e_y)$$

$$e_y = \frac{S_y}{E^*}$$

Residual term

$$F_i = \frac{1}{2\Delta X^2}\left\{\begin{array}{l}\left[\left(\frac{\bar{\rho}_c H^3}{\bar{\eta}}\right)_{i+1} + \left(\frac{\bar{\rho}_c H^3}{\bar{\eta}}\right)_i\right][g(\theta-1)]_{i+1} \\ -\left[\left(\frac{\bar{\rho}_c H^3}{\bar{\eta}}\right)_{i+1} + 2\left(\frac{\bar{\rho}_c H^3}{\bar{\eta}}\right)_i + \left(\frac{\bar{\rho}_c H^3}{\bar{\eta}}\right)_{i-1}\right][g(\theta-1)]_i \\ +\left[\left(\frac{\bar{\rho}_c H^3}{\bar{\eta}}\right)_i + \left(\frac{\bar{\rho}_c H^3}{\bar{\eta}}\right)_{i-1}\right][g(\theta-1)]_{i-1}\end{array}\right\}$$
$$-\frac{\psi}{\Delta X}\left\{\begin{array}{l}(1-\Phi)\left[(\theta\bar{\rho}_c H)_{i+1} - (\theta\bar{\rho}_c H)_i\right] \\ +(\Phi)\left[(\theta\bar{\rho}_c H)_i - (\theta\bar{\rho}_c H)_{i-1}\right]\end{array}\right\}$$
$$-\psi\frac{R_x(\theta\bar{\rho}_c)_i}{b}S^*$$

References

1. Reynolds O (1886) On the theory of lubrication and its application to mr beauchamp tower's experiments, including an experimental determination of the viscosity of olive oil. Philos Trans R Soc 177:157–234
2. Swift W (1932) The stability of lubricating in journal bearings. Proc Inst Civil Eng 233:267–288
3. Stieber W (1933) Hydrodynamische theorie des gleitlagers. Das Schwimmlager, V.D.I Verlag, Berlin
4. Elrod HG (1981) A cavitation algorithm. J Lubr Technol 103:350–354
5. Chong WWF, Teodorescu M, Vaughan ND (2011) Cavitation induced starvation for piston ring/liner tribological conjunction. Tribol Int 44(4):483–497
6. De la Cruz M, Chong WWF, Teodorescu M, Theodossiades S, Rahnejat H (2012) Transient mixed thermo-elastohydrodynamic lubrication in multi-speed transmissions. Tribol Int 49:17–29
7. Chong WWF, Teodorescu M, Rahnejat H (2013) Mixed thermo-elastohydrodynamic cam-tappet power loss in low-speed emission cycles. Int J Engine Res. doi:10.1177/1468087412461631
8. Patir N, Cheng HS (1978) An average flow model for determining effects of three-dimensional roughness on partial hydrodynamic lubrication. ASME J Lubr Technol 100:12–17
9. Patir N, Cheng HS (1979) Application of average flow model to lubrication between rough sliding surfaces. ASME J Lubr Technol 101:220–230
10. Rahmani R, Mirzaeeb I, Shirvanic A, Shirvanic H (2010) An analytical approach for analysis and optimisation of slider bearings with infinite width parallel textures. Tribol Int 43:1551–1565
11. Morris N, Rahmani R, Rahnejat H, King PD, Fitzsimons B (2012) The influence of piston ring geometry and topography on friction. Proc IMechE Part J 227:141–153
12. Greenwood JA, Williamson BP (1966) Contact between nominally flat surfaces. Proc R Soc Ser A 24:300–319
13. Greenwood JA, Tripp JH (1970) The contact of two nominally flat rough surfaces. Proc IMechE 185:625–633
14. Fuller KNG, Tabor D (1975) The effect of surface roughness on the adhesion of elastic solids. Proc R Soc Lond Ser A 345(1642):327–342
15. Johnson KL, Kendall K, Roberts AD (1971) Surface energy and the contact of elastic solids. Proc R Soc Lond Ser A 324(1558): 301–313
16. Chang WR, Etsion I, Bogy DB (1988) Static friction coefficient model for metallic rough surfaces. J Tribol 110:57–63
17. Polycarpou AA, Etsion I (1998) Static friction of contacting real surfaces in the presence of sub-boundary lubrication. J Tribol 120:296–303
18. Kogut L, Etsion I (2002) Elastic-plastic contact analysis of a sphere and a rigid flat. J Appl Mech 69:657–662
19. Kogut L, Etsion I (2003) Adhesion in elastic-plastic microcontact. J Colloid Interface Sci 261:372–378
20. Derjaguin BV, Muller VM, Toporov YP (1975) Effect of contact deformation on the adhesion of elastic solids. J Colloid Interface Sci 53:314–326

21. Shi X, Polycarpou A (2005) An elastic-plastic hybrid adhesion model for contacting rough surfaces in the presence of molecularly thin lubricant. J Colloid Interface Sci 290:514–525
22. Maugis D (1996) On the contact and adhesion of rough surfaces. J Adhes Sci Technol 10(2):161–175
23. Jackson RL, Green I (2005) A finite element study of elastoplastic hemispherical contact against a rigid flat. Trans ASME J Tribol 127:343–354
24. Green I (2005) Poisson ratio effects and critical values in spherical and cylindrical hertzian contacts. Int J Appl Mech 10:451–462
25. Vijaywargiya R, Green I (2007) A finite element study of the deformation, forces, stress formation, and energy loss in sliding cylindrical contacts. Int J Non-Linear Mech 42:914–927
26. Yan W, Komvopoulos K (1998) Contact analysis of elastic-plastic fractal surfaces. J Appl Phys 84(7):3617–3624
27. Morrow CA, Lovell MR (2005) A solution for lightly loaded adhesive rough surfaces with application to mems. J Tribol 127:206–212
28. Chong WWF, Teodorescu M, Rahnejat H (2013) Nanoscale elastoplastic adhesion of wet asperities. Proc IMechE Part J. doi:10.1177/1350650112472142
29. Chong WWF, Teodorescu M, Rahnejat H (2012) Formation of ultra-thin bi-molecular boundary adsorbed films. J Phys D 45(11):115303
30. Chong WWF, Teodorescu M, Rahnejat H (2012) Physiochemical hydrodynamic mechanism underlying the formation of thin adsorbed boundary films. Faraday Discuss 156:123–136
31. Andersson P, Koskinen S, Varjus S, Gerbig Y, Haefke H, Georgiou S, Zhmud B, Buss W (2007) Microlubrication effect by laser textured steel surfaces. Wear 262:369–379
32. Truhan JJ, Qu J, Blau PJ (2005) The effect of lubricating oil condition on the friction and wear of piston ring and cylinder liner materials in a reciprocating bench test. Wear 259:1048–1055
33. Costa HL, Hutchings IM (2007) Hydrodynamic lubrication of textured steel surfaces under reciprocating sliding conditions. Tribol Int 40:1227–1238
34. Deng HY, Wuang W, Wang X (2011) The effect of dimple shapes on friction of parallel surfaces. Proc IMechE Part J 225:693–703
35. De la Cruz M, Gore M, Morris N, Rahnejat H (2012) The role of laser surface textured patterns on friction in reciprocating contacts. Proceedings of ASME/STLE 2012 International Joint Tribology Conference. Denver, Colorado, IJTC2012:61149
36. Roelands CJA (1966) Correlational aspects of the viscosity–temperature–pressure relationships of lubricating oils. PhD Thesis, Technische Hogeschool te Delft, Netherlands
37. Dowson D, Higginson GR (1966) Elastohydrodynamic lubrication: the fundamentals of Roller and Gear lubrication. Pergamon, Oxford
38. Eyring H (1936) Viscosity, plasticity, and diffusion as examples of absolute reaction rates. J Chem Phys 4:283
39. Jalali-Vahid D, Rahnejat H, Jin ZM (1998) Elastohydrodynamic solution for concentrated elliptical point contact of machine elements under combined entraining and squeeze-film motion. Proc IMechE Part J 212(6):401–411
40. Ryk G, Etsion I (2006) Testing piston rings with partial laser surface texturing for friction reduction. Wear 261:792–796
41. Buenviaje CK, Ge SR, Rafaillovich MH, Overney RM (1998) Atomic force microscopy calibration methods for lateral force, elasticity, and viscosity. Mater Res Soc Symp Proc 522:187–192